

# Deformations in wide, center-notched, thin panels, part II: finite element analysis and comparison to experimental measurements

**Jeffrey D. Helm**, MEMBER SPIE  
Lafayette College  
Department of Mechanical Engineering  
Easton, Pennsylvania 18042

**Michael A. Sutton**  
**Stephen R. McNeill**  
University of South Carolina  
Department of Mechanical Engineering  
Columbia, South Carolina 29208

**Abstract.** Finite element analyses, for comparison with the experimental measurements, were performed for each panel described in Part I. Results indicate that (a) for the 305- and 610-mm panels, the finite element predictions and global experimental measurements for two of the displacement components,  $U(x, y, 0.80 \text{ mm})$  and  $W(x, y, 0.80 \text{ mm})$ , are in good agreement throughout the panel, (b) for the 305- and 610-mm panels, the finite element predictions for the vertical displacement field  $V(x, y, 0.80 \text{ mm})$  are  $\sim 5\%$  lower than the measurements throughout the panel, (c) for the 1016-mm panel, the finite element predictions did not match the experimental measurements due to the specimen slipping in the grip fixtures, as shown in the full-field measurements, resulting in significant changes in the measured panel deformations, and (d) for all three panels, the local finite element predictions for the in-plane strain components,  $\epsilon_{xx}$ ,  $\epsilon_{xy}$ , and  $\epsilon_{yy}$ , including the overall trends in both the size and shape of the large strain regions, are in quantitative agreement with experimental results. In summary, results indicate that an appropriate finite element method, capable of predicting the deformations observed in the structures to be modeled, will be effective in modeling the overall behavior of wide, flawed panels up to the onset of flaw growth. Furthermore, the combination of finite element analysis and three-dimensional measurements for accurate prediction of displacement boundary conditions is shown to be a viable hybrid approach for predicting flawed panel response. © 2003 Society of Photo-Optical Instrumentation Engineers. [DOI: 10.1117/1.1566002]

**Subject terms:** center-notched wide aluminum panels; finite element model and predictions; 3-D digital image correlation and measurements; prediction-measurement comparisons.

Paper MET-02 received Aug. 17, 2002; revised manuscript received Nov. 15, 2002; accepted for publication Nov. 15, 2002.

## 1 Introduction

A goal of the US Aging Aircraft Program was to develop experimentally verified computational models capable of predicting the measured 25% reduction in residual strength observed by Forman and others in large center cracked panels when buckling is unconstrained. Since the crack growth and failure processes occur in the presence of complex, highly nonlinear, structural deformations, such as reported in Part I, quantitative verification of computational algorithms must utilize systems of comparable complexity.

As noted in Part I, Seshadri et al.<sup>1</sup> used the STAGS analysis code to predict the maximum load achievable in a wide, center-cracked panel. Specifically, his work showed that the predicted maximum load for (a) a fully constrained wide  $M(T)$  panel was within 5% of experimental observation and (b) an unconstrained wide  $M(T)$  panel having the same geometry deviated by 10% from the experimental data.

In related work, for a 610 mm wide fully constrained  $M(T)$  specimen, Gullerud et al.<sup>2</sup> used the finite element code WARP3D and overpredicted the maximum load dur-

ing crack growth by 8.5%. In addition, the authors provided preliminary data that indicate WARP3D is capable of predicting the deformations incurred by unconstrained panels under far-field loading. In a follow-up paper,<sup>3</sup> the authors presented the analysis of crack growth in thin, unconstrained  $M(T)$  specimens using large displacement, 3-D cohesive elements and four 20-noded brick elements through the thickness to model crack tunneling and improve their resolution of the local constraint variations. Their work demonstrated the ability of the algorithm to reasonably predict measured loads and measured crack extensions on the outside surface. Using the 3-D cohesive elements, the authors were able to identify and predict various 3-D effects leading to shape changes during loading. The authors were also able to predict various degrees of crack front tunneling using the 3-D cohesive elements, providing improved agreement with experimental measurements during the early stages of crack growth.

Schultheisz, Pfaff, and Knauss performed both crack tip measurements using optical interferometry and detailed 3-D finite element analysis to assess the accuracy of finite element methods when predicting near-crack-tip deforma-

tions in relatively small three-point-bend fracture specimens machined from 4340 steel. Their results indicated that (a) the finite element analysis (FEA) results and measured deformations were in very good agreement for  $P/P_{max} < 0.75$ , even during the initial phases of crack growth and (b) the out-of-plane deformation measurements deviate from the FEA predictions earlier than the in-plane values.

The level of disagreement noted above<sup>1-3</sup> for the FEA of wide panels could be related to several factors, including (a) inherent computational inaccuracies for highly nonlinear, large displacement situations, (b) inability to model actual panel loading conditions, (c) inappropriate crack growth criteria, and/or (d) inaccuracies in modeling actual crack geometry. In an effort to identify the most likely source, the wide panel M(T) experiments described in Part I were performed to obtain full-field measurements regarding panel response *prior to crack extension*. The experimental database includes (a) load-displacement data, (b) full-field, global three-dimensional surface displacement data throughout the loading process, and (c) full-field, local strain data in the vicinity of the notch termination hole.

Since there is no reason to proceed with a numerical fracture simulation of wide, thin panels until simulations can be shown to adequately predict the stains and displacements prior to crack growth, this work presents detailed finite element analyses performed for thin, wide-panel specimens described in Part I. Section 2 presents an overview of the capabilities of the WARP3D algorithm, along with both the in-plane mesh geometry and boundary conditions used to model the panel specimens and the uniaxial  $\sigma$ - $\epsilon$  response for the 2024-T3 aluminum material used in the experimental program. Section 3 discusses the use of a nonplanar initial panel geometry to provide the deviation from symmetry necessary to predict the observed specimen deformations. Section 4 describes the convergence studies performed prior to finalizing the model geometry. Section 5 presents computational results for selected specimen geometries. Section 6 discusses the computational results. Section 7 compares experimental results and computational results. Section 8 provides remarks directed toward integrating the findings from both the experimental and computational studies. Section 9 provides general concluding remarks.

## 2 Finite Element Model Details

The panels studied for this work were modeled using the three-dimensional finite element code WARP3D. WARP3D was developed for the analysis of three-dimensional structures subjected to either static or dynamic loading. The code is capable of modeling contact, crack extension through nodal release and all displacement and loading boundary conditions. The element formulations within WARP3D support geometrically nonlinear analysis, with the ability to model the large displacements and rotations of particular importance in the wide M(T) panel analyses.

The program provides a choice of five different elements, including eight-node bricks, twenty-node bricks, and three transition elements. The models developed for this work used the twenty-node brick element designated *q3disop* in WARP3D. The *q3disop* element uses quadratic displacement functions. In this work, a mesh containing a single layer of *q3disop* elements through the half-thickness

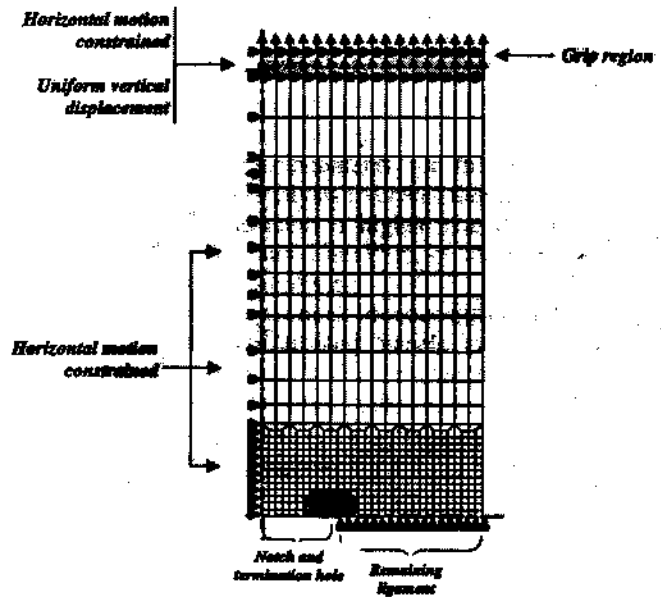


Fig. 1 In-plane panel geometry and boundary conditions for finite element models.

is used to estimate the through-thickness variations in deformation.<sup>1</sup> Though the level of refinement is less than used by previous authors<sup>2,3</sup> when modeling through-thickness tunneling and local variations in crack tip constraint during crack growth, our studies indicated that two elements through the thickness are adequate for our notched specimen that did not incur crack growth.

The general form of the finite element mesh used to model the 305-, 610-, and 1016-mm panels is shown in Fig. 1. The mesh geometry and imposed boundary constraints were produced using the mesh generation program PATRAN. The output from PATRAN was converted to the form required by WARP3D using the utility program PATWARP. The general mesh configuration shown in Fig. 1 was used for all three panels, with *mesh scaling* within PATRAN used to alter the physical dimensions to correspond with the 305-, 610-, or 1016-mm panel specimen.

For all analyses, the  $X,Y,Z$  coordinate system described in Part I, Section 4 and shown in Part I, Figure 7 is used, with the horizontal  $X$ -axis and vertical  $Y$ -axis intersecting at the point  $(0,0,Z=0)$  located at specimen mid-thickness. As shown in Fig. 1, symmetry about the  $YZ$  plane through the vertical centerline is imposed by  $U(X=0,Y,Z)=0$ . Symmetry about the  $XZ$  plane through the horizontal centerline is imposed by requiring  $V(X,Y=0,Z)=0$  for all nodes in the remaining ligament. Due to these symmetry conditions, a one-quarter specimen model is used in these numerical studies.

In the grip region, two rows of nodes in the grip elements were subjected to (a) a constant vertical displacement, (b)  $U(X_{grip},Y_{grip},Z_{grip})=0$ , and (c)  $W(X_{grip},Y_{grip},Z_{grip})=0$ , to emulate the same function as the portion of the specimen clamped in the grip of the test frame. To increase the vertical displacement of the grip, without altering the fixed constraints in the model definition, the *constraint scaling option* in the WARP3D program was utilized.

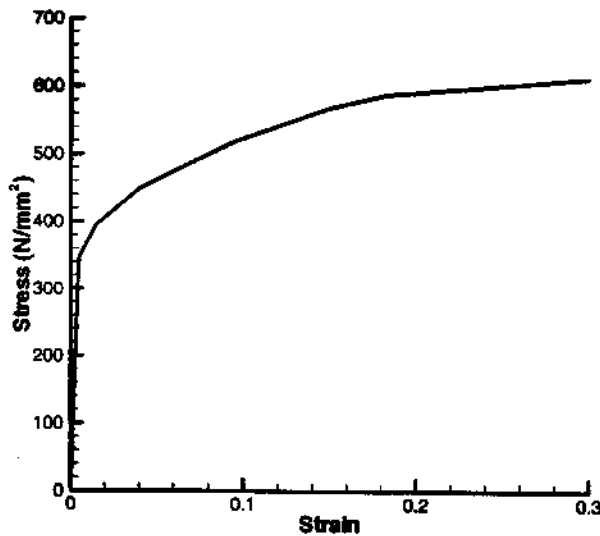


Fig. 2 Uniaxial stress-strain data for 2024-T3 aluminum.

The uniaxial  $\sigma$ - $\epsilon$  response for 2024-T3 aluminum is shown in Fig. 2. The data was input for analysis using the *piecewise linear* option in WARP3D. The stress values are given in  $\text{N}/\text{mm}^2$ , as required by WARP3D for consistency with the mesh dimensions in millimeters.

### 3 Initial Profile for Modeling

Though the computational code WARP3D can predict large deformation, it does not predict buckling from a perfectly planar initial state. Thus, the buckling effect observed in the experimental investigations does not occur in WARP3D if the modeled specimen is initially flat and the load is applied uniformly to the grip section of the specimen.

In order to model the buckling effect using WARP3D, the initial shape of the panel must be slightly "warped." To determine the effect of the initial profile shape on the displacement and strain fields, the three initial shapes shown in Fig. 3 were considered. The cosine shapes were selected based on the measured profiles for the 305- and 610-mm specimens. Similarly, the point perturbation is qualitatively similar to the measured shape for the 1016-mm panel. For each profile, the maximum deviation from planarity was 0.16 mm (1/10 the sheet thickness). To make the changes in the geometry visible in the figure the scaling factor for the Z direction has been exaggerated. Note that an additional set of panel analyses was performed using a planar specimen model, since the resulting predictions should be analogous to experiments performed with "perfect" antibuckling guides.

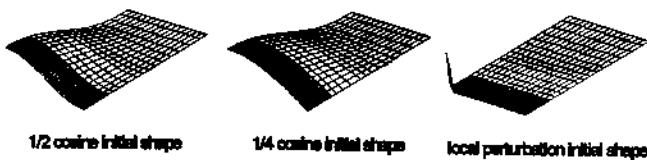


Fig. 3 Initial surface profile shapes for finite element modeling.

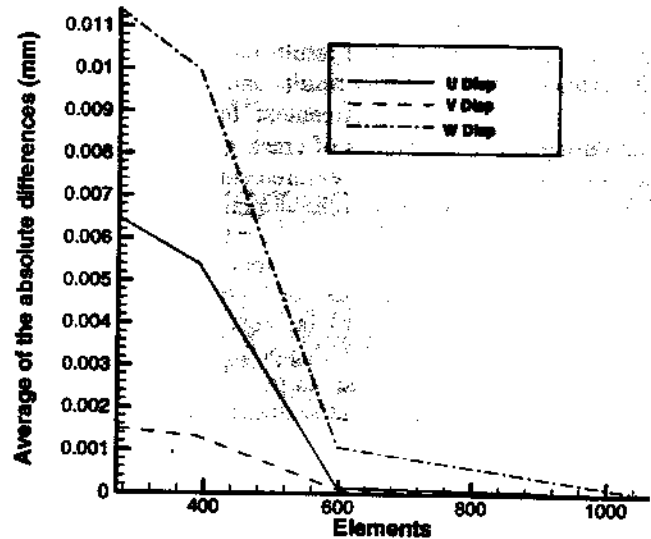


Fig. 4 Displacement-based convergence results for 610-mm panel.

### 4 Convergence Studies

A series of analyses was performed to determine both the required element size and also the allowable step size for the applied displacement so to assure convergence. The first convergence tests were performed for the 610-mm panel with the 1/2-cosine initial shape using 270, 390, 598, and 1064 elements, respectively.

As shown in Fig. 4, the displacement results for the 598-element mesh appear to be converged, with the displacement components (a) within 0.014% of the maximum  $U$  displacement of 1.0 mm, (b) within 0.005% of the maximum  $V$  of displacement of 2.0 mm, and (c) within 0.008% of the maximum  $W$  displacement of 14.0 mm obtained from the finite element analysis using 1064 elements. Because finite element analyses tend to converge in displacement faster than in stress, additional numerical simulations using mesh sizes up to 1264 elements were performed. Based on results from both the displacement and stress convergence studies, a mesh consisting of 790 elements and 5863 nodes was used to model all panel specimens.

Results from a series of analyses indicated that refining the initial displacement step size had very little effect on the final result of the analysis. At the step size chosen for all analyses, 0.025 mm per step, the average absolute difference in displacements was 0.30  $\mu\text{m}$  when compared to the displacements obtained with the smallest step size tested, 0.005 mm.

### 5 Numerical Simulation Results

#### 5.1 Initial Remarks

To aid in the comparison to experimental results presented later in this work, the coordinate system of the FEM analysis has been transformed into the coordinate system used to present the experimental data (see Part I, Sec. 4). In addition, since the quarter symmetry model assumes that the horizontal centerline of the panel does not move in the  $Y$  direction during loading, for each load step the  $V$  displacement imposed on the grip section is added to the FEM data's  $V$ -displacement field. All the experimental data was

taken on the lower half of the sheet, attached to the moving grip; this transformation compensates for the movement of the upper half of the panel and allows the direct comparison of the FEA and experimental data.

Also, it is worth noting the out-of-plane bending in each panel results in different displacement fields for the front and back of the panel. Thus, where appropriate, the full-field data for both sides of the specimen will be presented. When both are presented, the front of the panel is considered to be the side where values of the primary out-of-plane deformation are positive.

For the 305- and 610-mm panels, several analyses demonstrated that the initial shape used to induce buckling had no significant effect on the outcome of the analysis. Hence, only results from the 1/2-cosine and flat initial shapes will be presented for these models. For the 1016-mm model, a significant difference in the final results was obtained if the panel uses a 1/4-cosine initial flaw; these results will also be presented.

Finally, since comparison of the constrained and unconstrained model predictions at any load level gave similar results and insight, simulation results and comparisons are given only for the highest load level experienced by each panel.

## 5.2 Three-dimensional Displacement Fields at Maximum Load

Figures 5, 6, and 7 present the global, full-field  $U$ -,  $V$ -, and  $W$ -displacement field predictions, respectively. Each figure includes the predictions for the front and back of the 305-, 610-, and 1016-mm wide M(T) panels using the 1/2-cosine initial profile and also includes the results using a planar initial profile. While the contour colors and the contour line spacing are the same for all the plots for a particular field ( $u$ ,  $v$ , or  $w$ ), the scale of the  $x$  and  $y$  axis have been adjusted to an appropriate size for each panel size (305, 610, or 1016 mm).

## 6 Discussion of Finite Element Results

### 6.1 Numerical Simulation Results—Global Fields

The data in Figs. 5, 6, and 7 indicate that, when compared to the fields with buckling constrained, the deformations are quite similar on both the front and back of the thin panel specimen. The following discussion on the FEA results will be based on *front surface* predictions unless otherwise noted.

As shown in Figs. 5–7, the effect of constraining out-of-plane displacements on the deformation fields is clearly visible in the response of all three panels. For example, as shown in Fig. 5, by constraining out-of-plane motion the full width of the plate transfers the horizontal load in a relatively uniform way, resulting in a slowly varying transverse displacement field that is consistent with Poisson contraction effects. However, in unconstrained panels the maximum  $U$  displacement increased by more than a factor of two relative to flat plate predictions. As the center of the panel buckles out-of-plane, the free edge of the panel is free to move inward, with the buckled panel offering significantly less resistance to horizontal compressive stresses.

In contrast to the  $U$ -field results, the  $V$  fields shown in Fig. 6 are quite similar for all constrained and uncon-

strained panels. Here, the effects of the notch are dominant, with the primary difference between constrained and unconstrained panel  $V$ -field deformations being a higher grip displacement for the unconstrained panel. The increase is due to a reduction in longitudinal “stiffness” caused by higher out-of-plane displacements for the unconstrained panel. In addition, the analysis indicates that the gradient in notch opening displacement is higher near the end of the notch for the unconstrained analysis, as the warped panel tends to increase notch opening.

As shown in Fig. 7, the most obvious difference between unconstrained and constrained panels is the complex, highly nonlinear, warping of the thin panels that continues all the way to the grip region, with the largest out-of-plane displacement fields near the notch centerline. This is due to plate bending effects introduced by the initial profile and compressive  $\sigma_{xx}$  stresses in the area above and below the notch.

Further review of Fig. 7 shows that increasing panel size results in different structural shapes; a single maximum for the 305-mm panel, a maximum and a minimum for the 610-mm panel, and a compressed maximum and minimum followed by a relatively flat area near the free edge for the 1016-mm panel.

While it is generally true that the front and back of the panel exhibit approximately the same response when compared to the constrained panel model, differences in the  $U$  displacements for the front and back of the panel indicate the influence of the bending of the panel. Figure 8 shows a line of data from the horizontal centerline of the 305-mm panel for both the front and back of the panel. Although the Poisson effect produces horizontal compressive stresses in the center of the panel, the bending stresses produced by panel warping are high enough to cause a net tensile stress at the center of the panel’s front plane. This effect can be seen in the positive slope of the  $U$  displacements in the center of the panel’s front plane; since bending produces compressive stresses on the back side of the panel, the slope does not change sign for the back side of the panel.

Finally, though not shown in Fig. 7, analytical results for the 1016-mm panel using an initial 1/4-cosine initial shape resulted in a completely different deformed shape. Figure 9 shows the two deformed shapes. Though the deformed shape obtained using the 1/4-cosine profile was not observed in any experiments that were carried out for the Aging Aircraft Program, it is noted that (a) the in-plane displacement fields produced by this structural shape are in reasonable agreement with those predicted for an unflawed panel and (b) the out-of-plane field is much less severe. This suggests that if an actual panel deformed into this shape, it may have greater residual strength than panels that experienced the experimentally observed buckling pattern.

### 6.2 Numerical Simulation Results—Local Strain Fields

As shown in Fig. 10, the predicted strain fields for unconstrained and constrained panels have similar overall trends. However, closer inspection of the data indicates that the unconstrained panel has higher overall strains. Specifically, the following are noted:

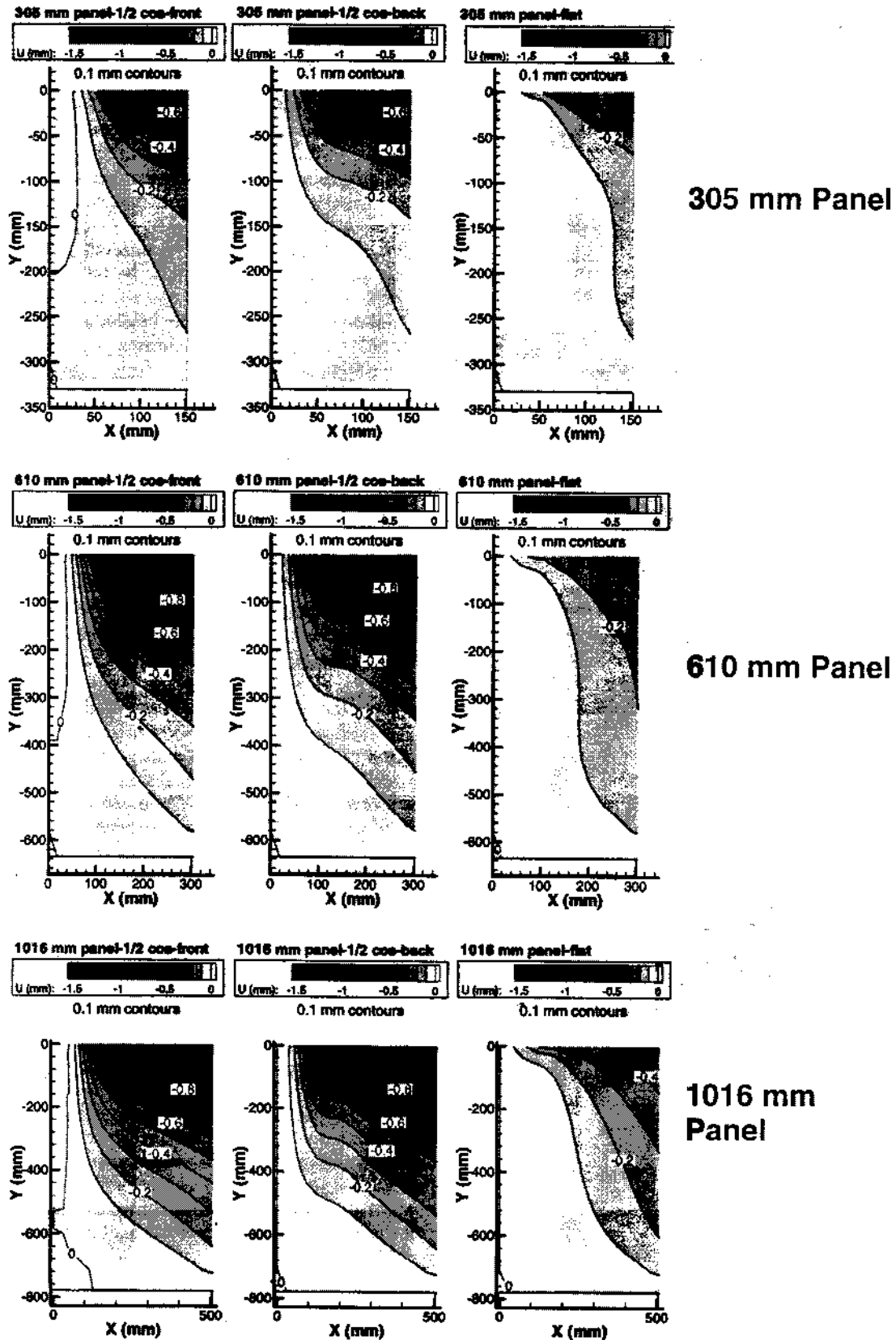


Fig. 5  $U$ -displacement fields for all panels at maximum load.

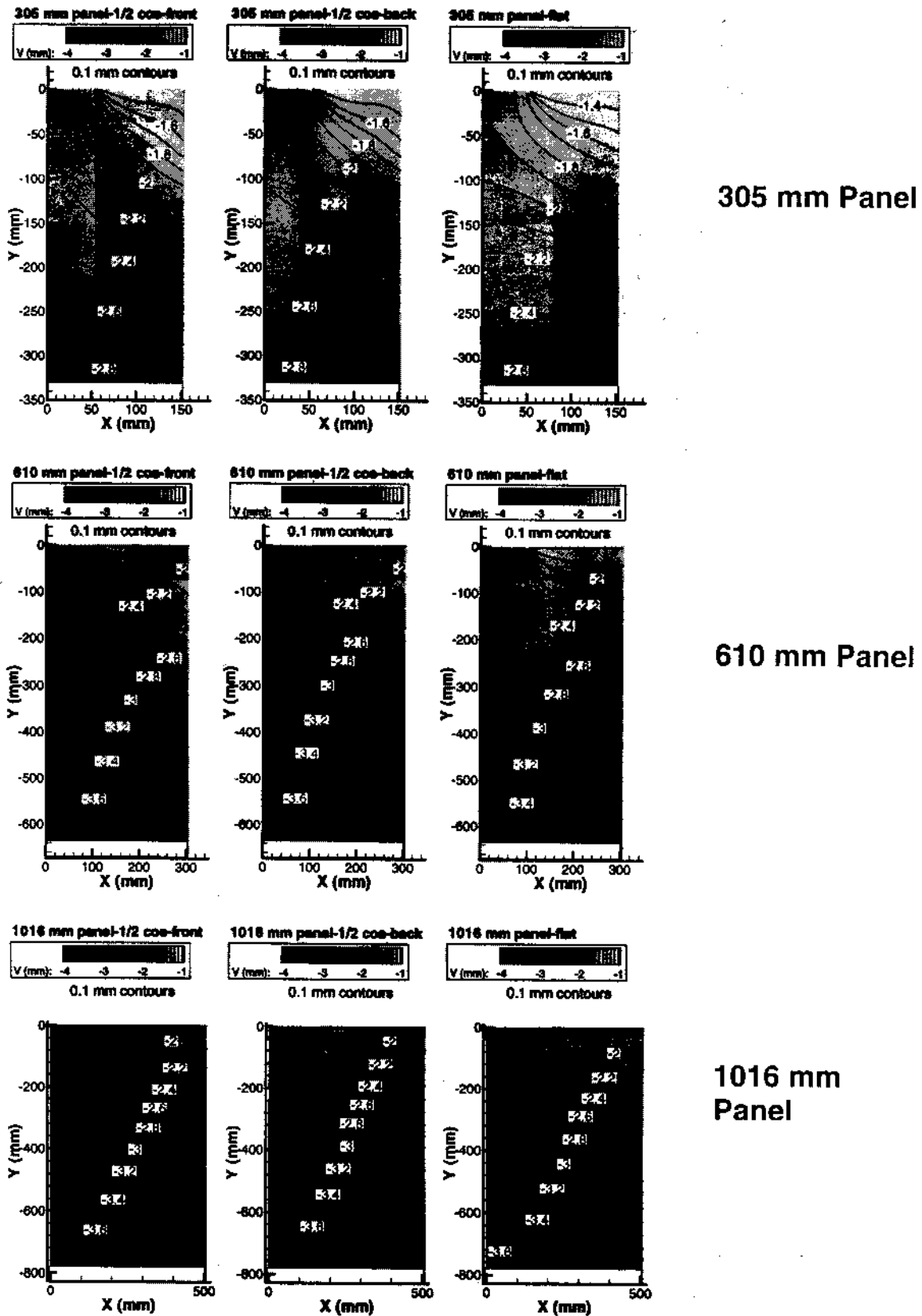


Fig. 6 V-displacement fields for all panels at maximum load.

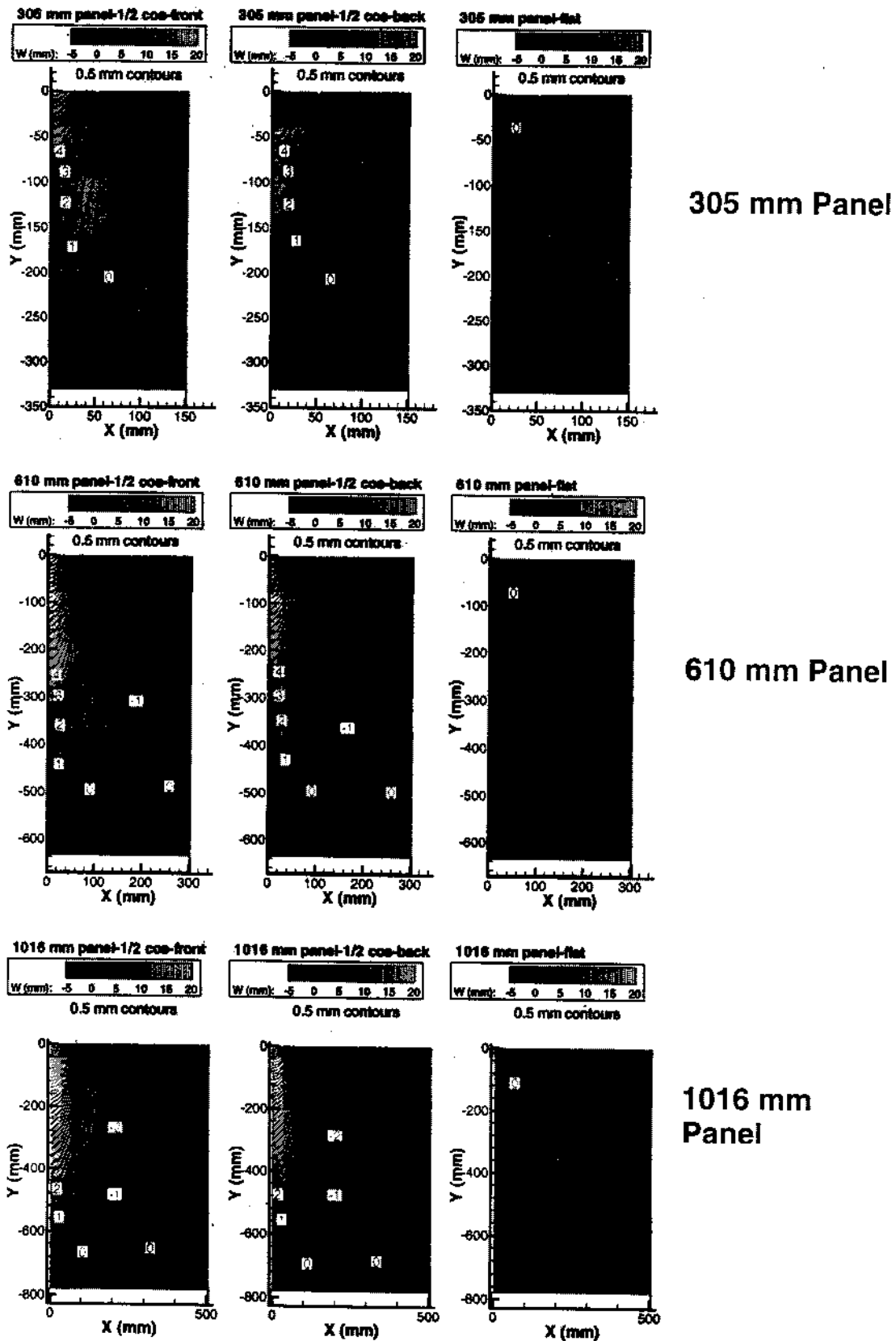


Fig. 7 W-displacement fields for all panels at maximum load.

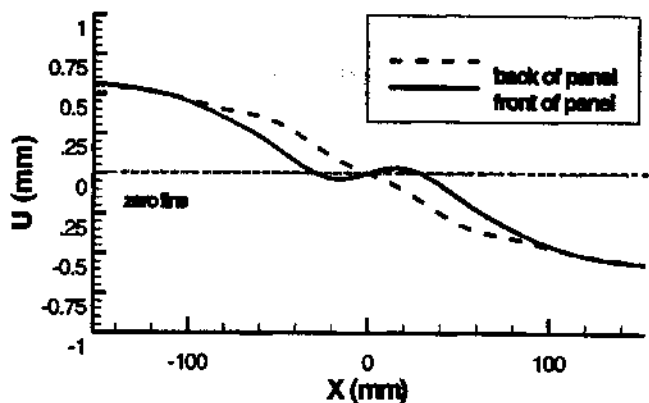


Fig. 8  $U$ -displacement predictions along the horizontal centerline on both front and back surfaces.

1. The maximum  $\epsilon_{yy}$  strain for the unconstrained panel is 0.29, which is more than 50% larger than predicted for the constrained panel.
2. The physical size of the high strain region is larger for the unconstrained panels, which is particularly evident when comparing the  $\epsilon_{xx}$  and the  $\epsilon_{xy}$  fields.

Thus, by eliminating constraint in a thin panel, the analysis predicts that one effect is an elevation in the strain fields around discontinuities such as the notch termination hole in these studies; this is consistent with the experimentally observed reduction in residual strength of unconstrained panels.

## 7 Comparison of FEA and Experimental Data

This section will present a comparison of the finite element predictions to the experimental results from Part I of this work. Because it is not possible to know a priori which direction the experimental panels will warp, and, as discussed in Sec. 6, there are differences in the behavior of the front and back of the panels, the comparison with experimental results will be presented for the measured side of the panel. Thus, data will be presented for (a) the back of the 305- and 610-mm panels and (b) the front of the 1016-mm panel. The comparison is provided as displacement data along three horizontal lines on the panel, with the position of the line measured vertically from the notch line. The graph lines are generated from (a) the experimental data, (b) the appropriate side of the unconstrained analysis

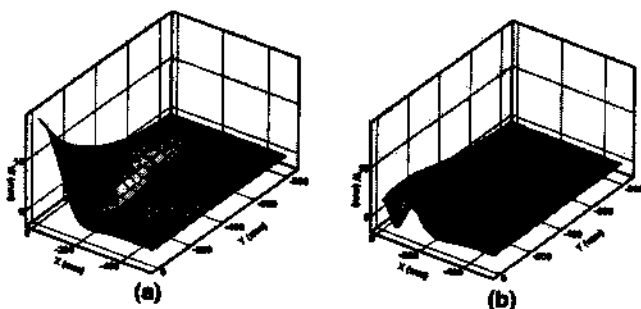


Fig. 9 Deformed shape of 1016-mm panel with (a) 1/2-cosine initial shape and (b) 1/4-cosine initial shape.

with an initial profile, and (c) the constrained analysis with a flat panel. These graphs are presented for three load levels for each of the panels. The results for the 305-, 610-, and 1016-mm panels are presented in Figs. 11, 12, and 13. Where necessary the FEA data have been extended, using the 1/4-plate symmetry, to cover the entire width of the specimen.

Because of the concern over the slipping of the panel grip section for the 1016-mm panel, as discussed in Part I, a line of data was extracted as close to the grip edge as possible, 46 mm above the grip, from the data set for the maximum load (236 kN). This data is compared to FEM data at the same location in Fig. 14. To enhance the comparison in the  $V$  displacements the displacement of the central point was subtracted from the rest of the data. As shown in these graphs, the displacements clearly differ from those predicted by the FEM, and are larger than expected less than 50 mm from the grip. This further supports the assertion that the outer edges of the panel were slipping while the load was applied.

Figure 15 presents a direct comparison between the local strain fields for the FEA and experimental results at maximum load for the 305-mm panel. The comparison is for a 15-mm-square region containing the notch termination hole, with the FEA results from the front side (the side with the local camera system) of the panel. Only one comparison is provided since similar results were obtained for all three panels.

## 8 Discussion of FEA and Experimental Results

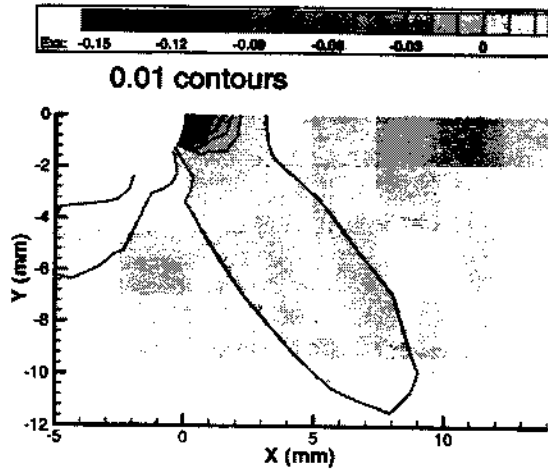
Inspection of Figs. 11–13 shows that, relative to unconstrained specimens, the results for all constrained panels have much smaller gradients throughout the field, especially as the load increases. Furthermore, for larger load levels, the constrained panel results do not agree with either the experimental data or the unconstrained panel simulations. As such, the flat panel data will not be emphasized in the remainder of this section.

As shown in Figs. 11 and 12, for low and moderate tensile loading there is general agreement between FEA predictions and experimental measurements for the 305- and 610-mm panels, with only a slight reduction in vertical displacement for the flat panel predictions. At maximum loading, there is very good agreement for the  $U$  and  $W$  components of displacement between the FEA results using an initial profile and the experimental data. However, the  $V$ -displacement results for the unconstrained panel are somewhat lower than the experimental measurements, suggesting that the FEA model may be slightly too stiff in this direction.

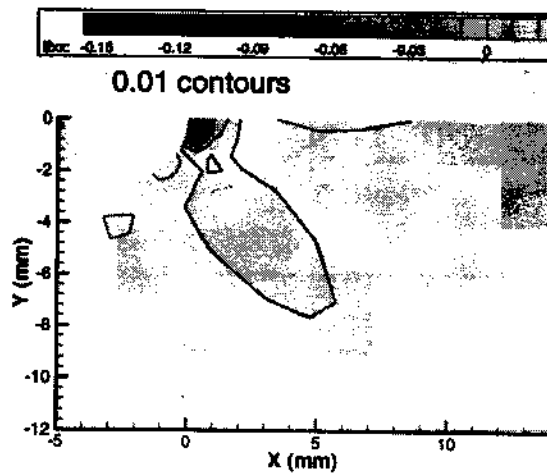
As noted in Part I, the 1016-mm panel appeared to slip out of the grip under tensile loading. As shown in Fig. 14, the slippage is clearly visible at the edge of the panel. Here, as one approaches the free-edge of the specimen along the line closest to the grip, both the experimental  $U$ -displacement fields and the  $V$ -displacement field near the grip are much larger than predicted by the unconstrained panel FEA.

As shown in Fig. 15, there is very good agreement between the unconstrained FEA specimen predictions and the experimental results for the in-plane strain components  $\epsilon_{xx}$ ,  $\epsilon_{xy}$ , and  $\epsilon_{yy}$ ; the overall trends in both the size and

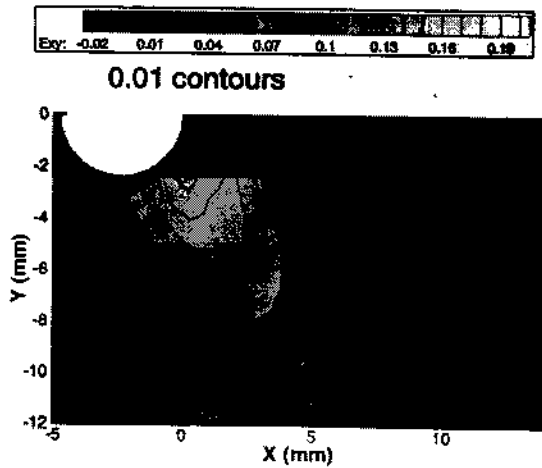
**Exx - 1/2 cosine panel front**



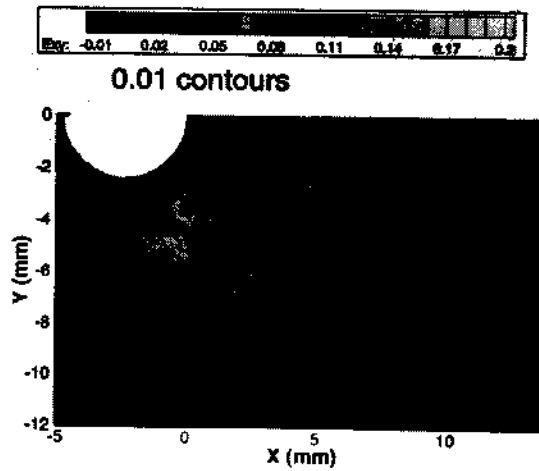
**Exx - flat panel**



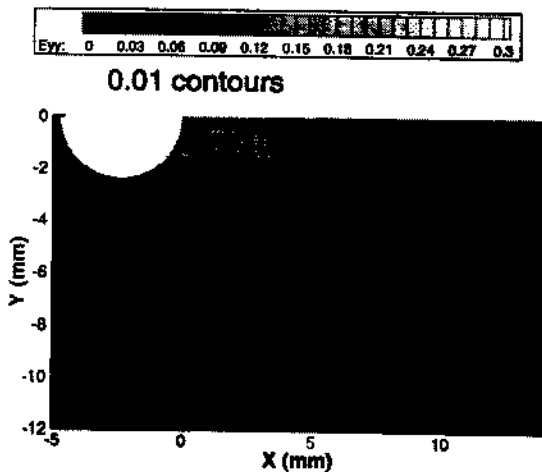
**Exy - 1/2 cosine panel front**



**Exy - flat panel**



**Eyy - 1/2 cosine panel front**



**Eyy - flat panel**

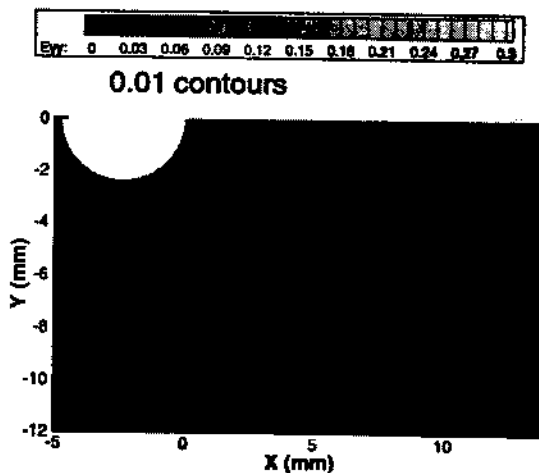


Fig. 10 Comparison of predicted local strain fields for 305-mm panel for 1/2-cosine and flat initial shapes.

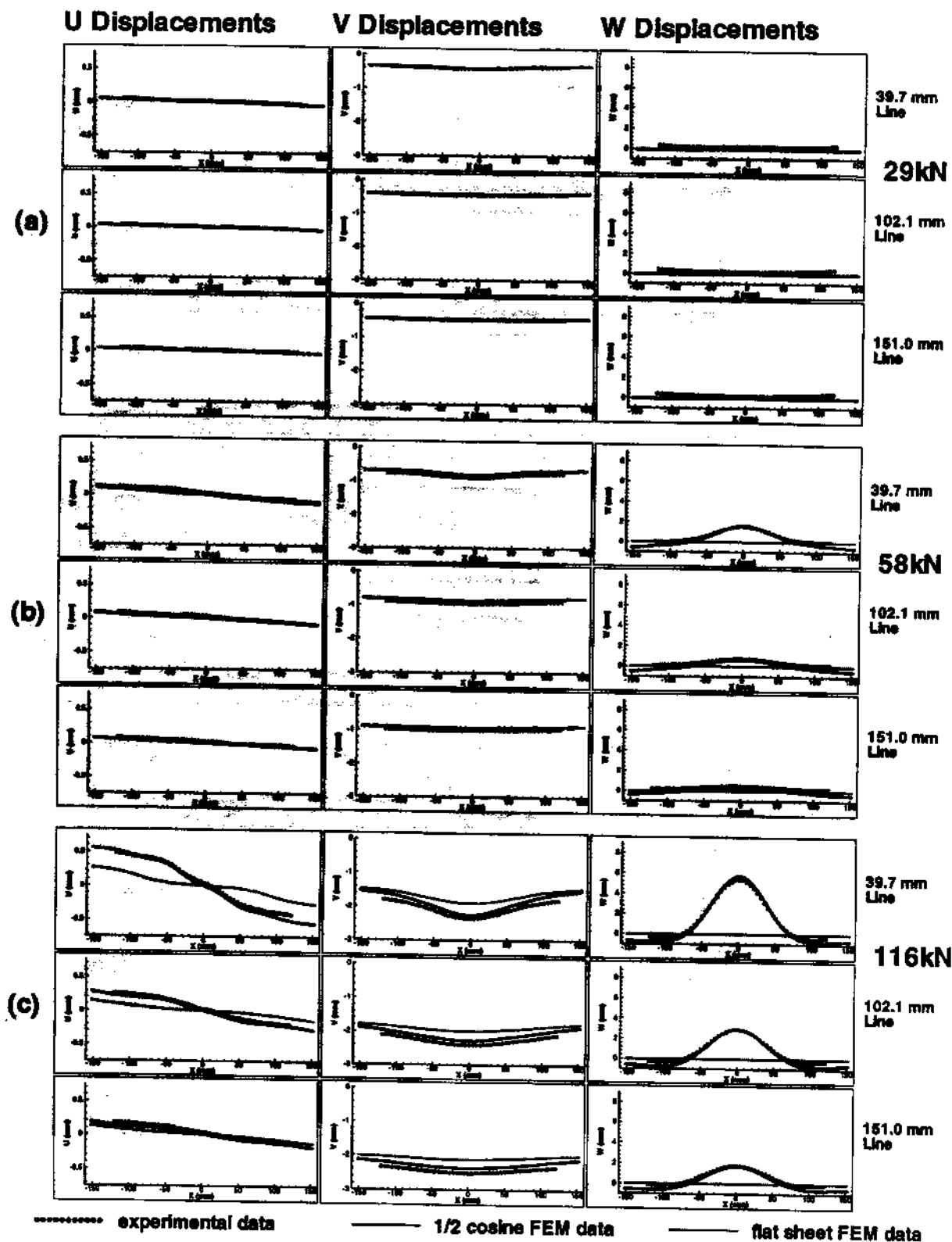


Fig. 11 Comparison of FEM and experimental data along horizontal lines in 305-mm panel for three tensile loading levels.

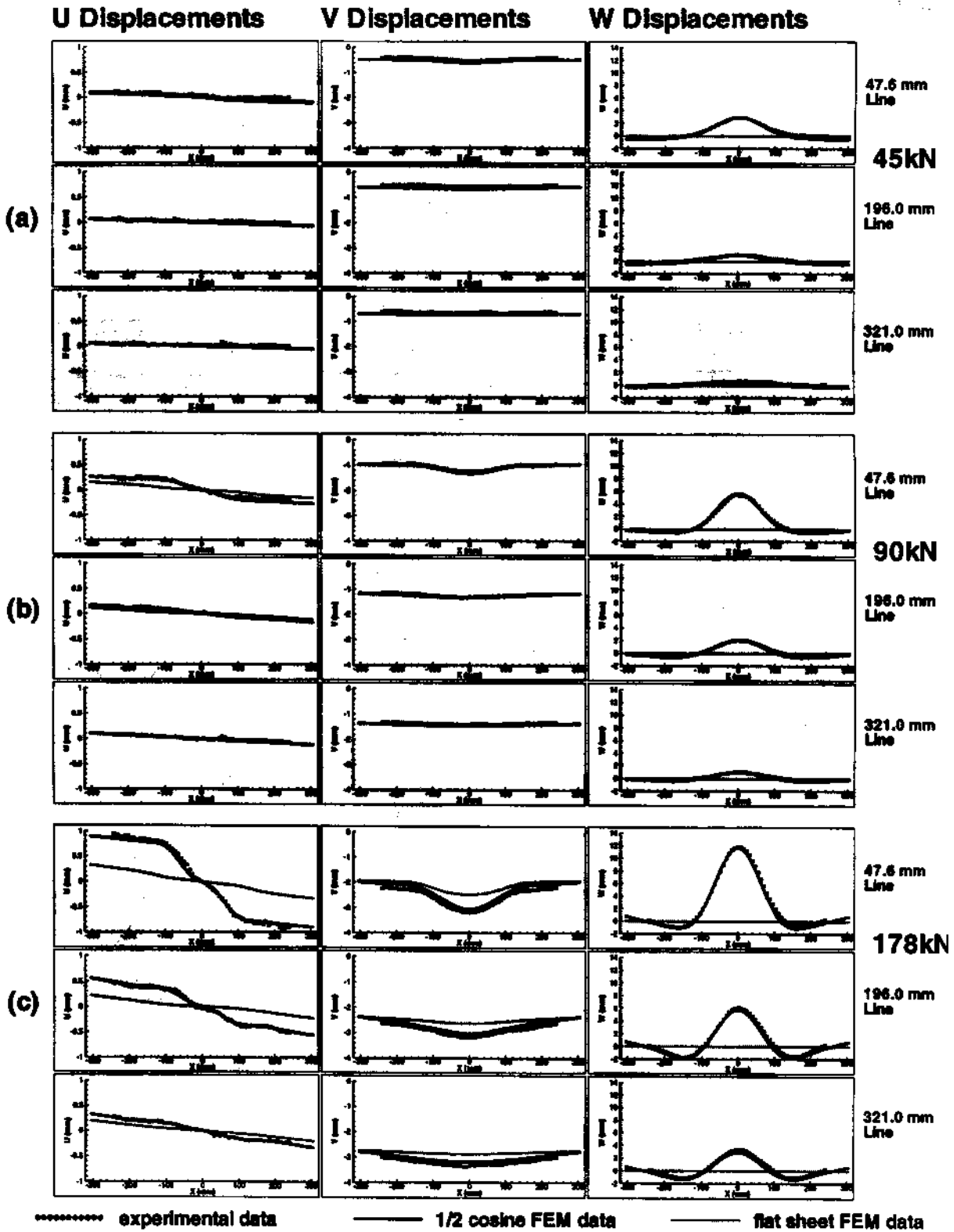


Fig. 12 Comparison of FEM and experimental data along horizontal lines in 610-mm panel for three tensile loading levels.

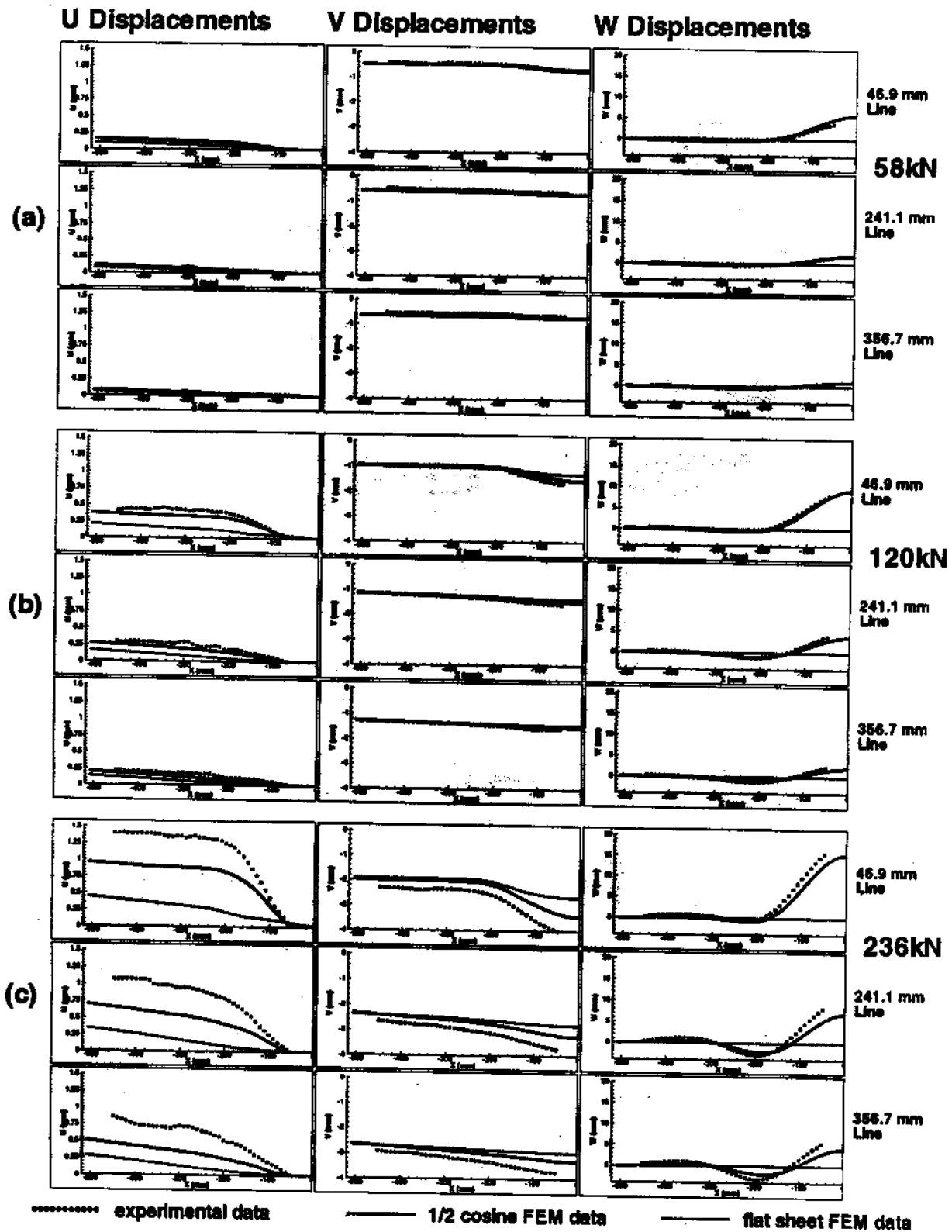


Fig. 13 Comparison of FEM and experimental data along horizontal lines in 1016-mm panel for three tensile loading levels.

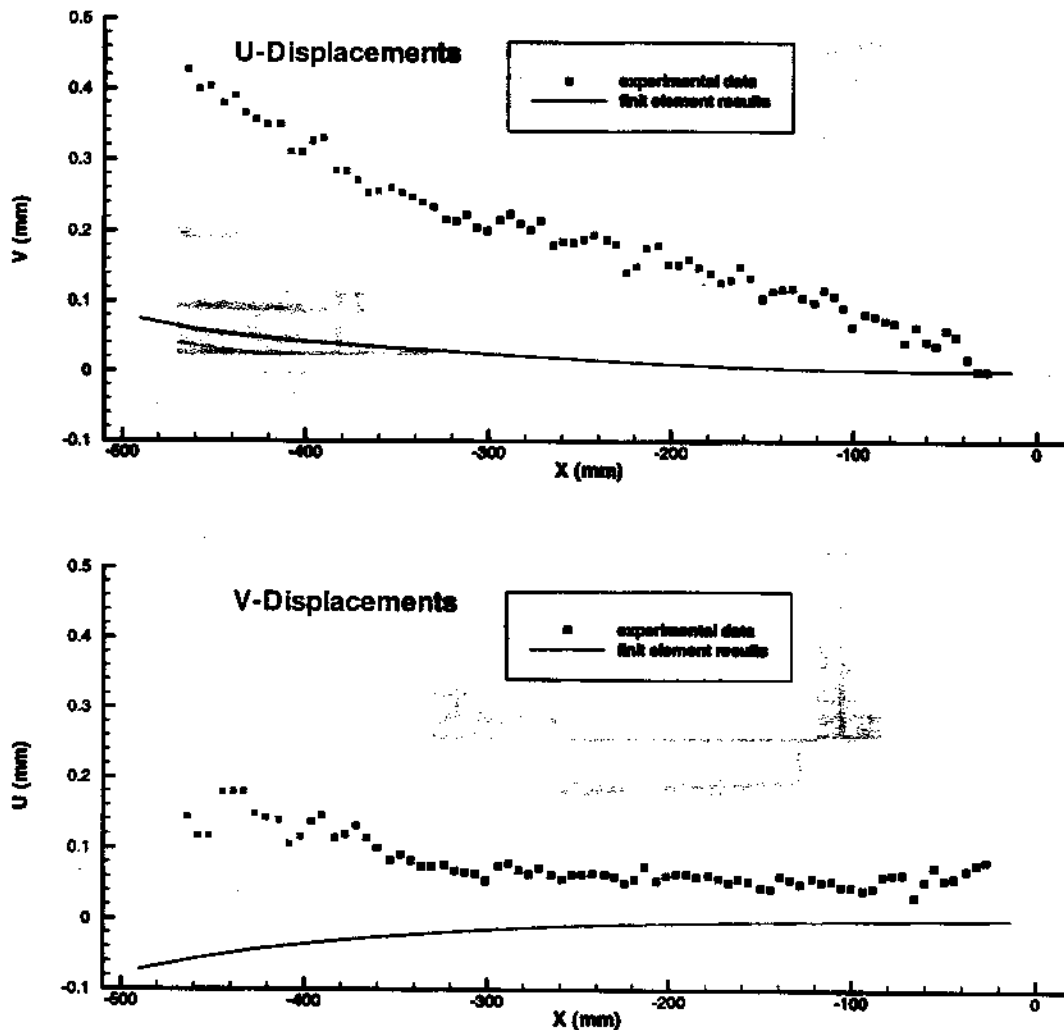


Fig. 14 Comparison of  $U$  and  $V$  displacement 46 mm above the grip line for the 1016-mm panel.

shape of the larger strain regions are in quantitative agreement between experiment and model predictions.

## 9 Concluding Remarks

The numerical study presented herein provides initial results assessing the capabilities of modern FEA codes to predict the precrack growth behavior that will eventually govern the fracture response of a material-structure system. More generally, the authors believe that the work demonstrates the robustness of a combined numerical-experimental methodology for validation of numerical predictions, especially when full-field, 3-D displacement and deformation measurements are used in the simulation evaluation process.

Specifically, a direct comparison of Figs. 9–11 in Part I to Figs. 5–7 in Part II, as well as the line comparisons in Figs. 11–13 in Part II, indicate that the FEA solutions using WARP3D are in good agreement with global experimental measurements. In particular, the close agreement between the  $U$  and  $W$  fields indicates that the FE model is accurately representing the bending response of the structure. It is noted that, in this regard, there is general agreement with the results from previous work,<sup>4–6</sup> where the authors showed excellent agreement between FEA and experiments

up to 75% of the maximum loading. Conversely, the modest underprediction of vertical displacement field in this work suggests that the FE model is somewhat stiff when representing this deformation state.

Careful inspection of the results in Fig. 15 indicate that there are strain differences very close to the hole diameter, ranging from 0.005 for  $\epsilon_{xy}$  to 0.015 for  $\epsilon_{xx}$ . Based on our studies, there appear to be two main factors that account for these differences. The first involves the conversion of the experimental displacement data to strains. As explained in Part I, the strain conversion involves the fitting of a third-order surface to the experimental data. In areas where the fields change quickly, and in a manner that may not be well approximated by a third-order surface, the method will have a tendency to average the strain. The second involves the difficulty that FEM methods traditionally have at points that are constrained, and at local stress concentrations, conditions particularly evident at the leading edge of the hole. The agreement of the finite element results and the experimental data in areas further away from the edge of the hole suggests that additional studies may be required to resolve the source of the discrepancies. This may be possible with (a) higher magnification to obtain additional data near the hole diameter, thereby reducing the averaging effect for the

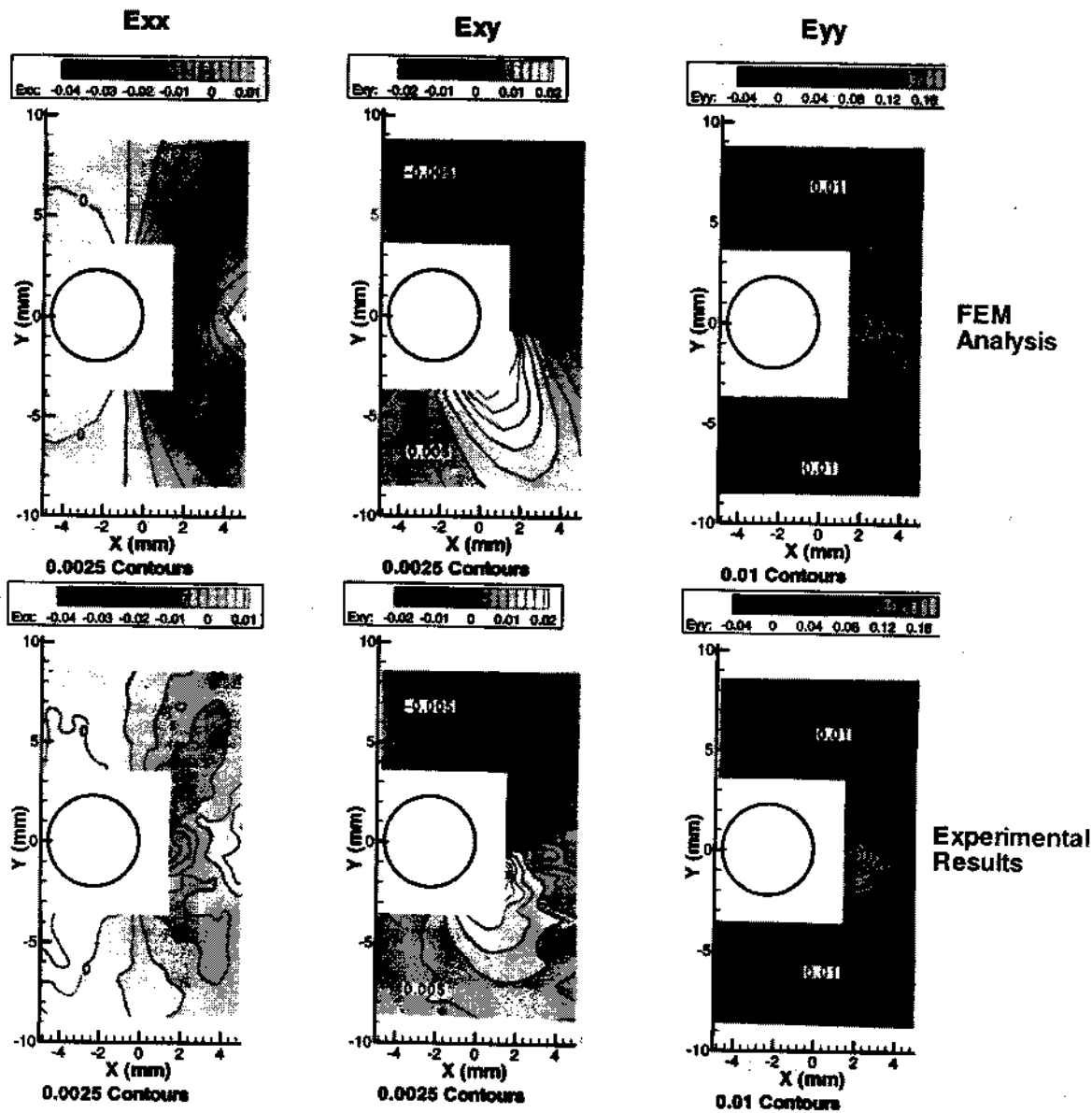


Fig. 15 Comparison of FEM and experimental strain fields near termination hole at maximum load for a 305-mm panel.

experimental strains and (b) refinements in the local mesh for the finite element analysis to diminish the effect of the constraints and stress concentrations.

With regard to previous work,<sup>4-6</sup> which indicated that the best agreement in the crack tip fields was for loading below 75% of the maximum load, the wide-panel studies do not indicate that there is any quantitative change in the level of agreement with loads up to 100% of the maximum load. Since additional studies are required for a valid comparison of experimental results and FE predictions near the termination hole, a direct comparison to results near a crack tip in Refs. 4-6 is not considered in this work.

As noted previously, the 3-D displacement measurements were used to identify variances from the assumed experimental boundary conditions in the gripping portion of the panels. For such cases a hybrid approach,<sup>7-10</sup> whereby independent, experimental measurements are used

to define the actual boundary conditions for FEA (e.g., the three-dimensional displacement fields obtained using stereovision and digital image correlation algorithms), is required to accurately predict panel deformations and stresses. It is important to note that the use of three-dimensional displacement data in such a hybrid finite element approach would allow the direct comparison of finite element results to experimental data where the imposition of specific edge conditions may be difficult if not impossible. This would free the validation of finite element code from rigidly controlled experiments and allow the study of the more complex structures and loadings, the very situations where FEM analysis is typically employed.

Results from our studies confirm that an appropriate FEA is fully capable of predicting the complex deformations that occur in thin plates up to the onset of crack growth. Since previous analyses<sup>1-3</sup> have indicated larger

errors when attempting to predict the stable tearing process up to maximum load (e.g., residual strength predictions), our results strongly suggest that the primary source of inaccuracies in predicting residual strength is in the prediction of the direction and onset of stable tearing. Thus, provided that a physically realistic, verified fracture criterion has been developed for the material of interest, then the use of FEA algorithms such as WARP3D with established methods for releasing nodes and allowing crack growth along arbitrary directions should provide a viable method for predicting residual strength.

### References

1. B. R. Seshadri, J. C. Newman, Jr., D. S. Dawicke, and R. D. Young, "Fracture analysis of the FAA/NASA wide stiffened panels," Second Joint NASA/FAA/DoD Conf. on Aging Aircraft (Jan. 1999).
2. A. Gullerud, R. Dodds, R. Hampton, and D. Dawicke, "3-D modeling of ductile crack growth in thin metals: computational aspects and validation," submitted to *Eng. Fract. Mech.* 63, 347-374 (1999).
3. S. Roychordhury, Y. D. ArunRoy, and R. H. Dodds, Jr., "Ductile tearing in thin aluminum panels: Experiments and analyses using large-displacement, 3-D surface cohesive elements," *Engr. Fract. Mech.* 69(8), 983-1002 (2002).
4. C. R. Schultheisz, R. D. Pfaff, and W. G. Knauss, "An experimental/analytical comparison of three-dimensional deformations at the tip of a crack in a plastically deforming plate—part II: material characterization and finite element analysis," *Int. J. Fract.* 90(1-2), 27-46 (1998).
5. C. R. Schultheisz, R. D. Pfaff, and W. G. Knauss, "An experimental/analytical comparison of three-dimensional deformations at the tip of a crack in a plastically deforming plate—part III: comparison of numerical and experimental results," *Int. J. Fract.* 90(1-2), 47-81 (1998).
6. K. C. Koppenhoefer, A. S. Gullerud, C. Ruggieri, R. H. Dodds, and B. E. Healy, "WARP3D release 11.0 dynamic nonlinear analysis of solids using a preconditioned gradient software architecture," (Nov. 1998).
7. M. A. Sutton, R. Howard, J. R. Dickerson, and S. R. McNeill, "A constrained least squares approach for the hybrid stress analysis of elastic bodies," *Eng. Anal. Boundary Elem.* 8(2), 58-68 (1991).
8. S. T. Lin and R. E. Rowlands, *Opt. Lasers Eng.* 32(3), 257-298 (1999).
9. J. Rhee, S. He, and R. E. Rowlands, "Hybrid moire-numerical stress analysis around cutouts in loaded composites," *Exp. Mech.* 36(4), 379-387 (1996).
10. H. H. Abdelmosen and R. E. Rowlands, "Hybrid stress analysis of flexed isotropic and composite plates," *Comput. Struct.* 44(5), 1017-1027 (1992).

Biographies and photographs of the authors appear in the paper "Deformations in wide center-notched, thin panels, part I: three-dimensional shape and deformation measurements by computer vision" in this issue.